Adiabatic behavior of an elliptical vortex in a time-dependent external strain flow

N. C. Hurst ⬤,* J. R. Danielson, D. H. E. Dubin, and C. M. Surko ⬤
*Department of Physics, University of California San Diego, 9500 Gilman Drive,
La Jolla, California 92093-0354, USA*

The adiabatic behavior of two-dimensional (2D) fluid vortices subject to slowly varying, time-dependent external strain flows is studied theoretically, and experimentally using magnetized non-neutral electron plasmas. Here the $\mathbf{E} \times \mathbf{B}$ drift dynamics of the electrons perpendicular to the magnetic field are analogous to the motion of fluid vorticity under the 2D Euler equations describing ideal fluids. A low-dimensional elliptical vortex patch model is used along with a WKB approximation to derive a formula for the breaking of an adiabatic invariant due to the changing external flow. The invariant is interpreted as the amplitude of a perturbative oscillation about a stable fixed point corresponding to a steady elliptical vortex. Smooth, hyperbolic tangent and piecewise linear ramp functions are considered for the external strain time dependence. Standard exponential breaking is observed in the former case, whereas the latter exhibits a power-law breaking curve with periodic modulation. It is found that a driving term in the equations of motion contributes the majority of the breaking whereas the frequency variation plays a weaker, but significant role. The experimental data agree closely with the theoretical model. The most significant deviation is due to inviscid damping behavior associated with the smooth edges of the experimental vortices, which tends to reduce the amplitude of the oscillation. The results are compared and contrasted with other related experimental, numerical, and theoretical work.

I. INTRODUCTION

Adiabatic behavior is a special case of time-dependent perturbation theory in both classical and quantum mechanics involving oscillatory systems with parameters that vary slowly in time [1–3]. In the classical regime, an approximate conservation law arises due to a separation between the oscillation period T and the characteristic timescale τ of the parameter variation. The conserved quantities are known as adiabatic invariants, and their defining feature is that the invariance is broken by an amount which approaches zero as $\tau/T \to \infty$. Adiabaticity provides a powerful constraint on rapid oscillatory motion across a broad range of systems, especially in cases with complicated time dependence that would otherwise render the problem intractable. These ideas have been particularly fruitful in the analysis of charged particle motion in the context of plasma physics and astrophysics [4–9], as well as in the fields of atomic physics [10] and fluid dynamics [11–13].

Here we consider the example of a rotating, two-dimensional (2D) fluid vortex subject to an externally imposed shear or strain flow which changes slowly in time. In the case of a piecewise-constant vorticity distribution known as a vortex patch [14] subject to a constant external flow, Moore and Saffman [15] and Kida [16] obtained exact solutions to the Euler equations describing

---

*Present address: Physics Department, University of Wisconsin—Madison; nhurst@wisc.edu

ideal (inviscid, incompressible) fluids. When the shear or strain rate is strong enough relative to the vorticity, the vortex is destabilized and stretched into a thin filament. For weaker external flows, the vortex patch can assume a steady elliptical shape or experience periodic elliptical distortions. When the shear or strain rate is taken to be a function of time, the resulting behavior can be complicated and possibly chaotic [17,18]. However, if the vortex rotates rapidly relative to its changing environment, then the tools of adiabatic theory can be employed. Exponential breaking of an adiabatic invariant related to Kida's periodic solutions [16] has been demonstrated using numerical simulations of vortex patches moving past boundary features [13]. The more complicated case of a vortex with a smooth, continuous vorticity profile has also been investigated numerically, showing that the outer layers are progressively stripped away by the external flow while the stable interior remains elliptical [11,12]. However, detailed modeling of the adiabatic breaking and experimental studies have not yet been conducted.

In this paper we report experimental investigations and theoretical analysis of the adiabatic behavior of an elliptical vortex in an ideal 2D fluid in response to an external strain flow where the strain rate is ramped upward in time. The data are acquired using pure electron plasmas in the laboratory, for which the $\mathbf{E} \times \mathbf{B}$ drift dynamics perpendicular to the magnetic field are analogous to those of an ideal 2D fluid, with electron density playing the role of fluid vorticity [19,20]. Exponential breaking of an adiabatic invariant related to periodic elliptical distortions of the vortex [16] is observed in response to a smooth, hyperbolic tangent ramp function. In the case of a piecewise linear ramp function, the breaking is described by a power-law envelope with periodic modulation, similar to the results of Refs. [7,8]. Using the Kida model of an elliptical vortex patch in an external flow [16,17,21] along with the WKB method, an expression is derived for the change in the invariant as a function of the ramp rate. In contrast with previous work [1,7,8,22], it is shown that the breaking is predominantly due to a driving term in the equations of motion, with frequency variation playing a weaker but significant role. The data are in close agreement with the model, except for a slight departure due to an inviscid damping effect [23–26] associated with the realistic smooth edges of the experimental vortices.

Ideal 2D fluids are among the simplest nonlinear fluid systems and therefore provide an important setting for understanding the dynamics of coherent flow structures and turbulence [27,28]. They are described by the Euler equations

$$\left(\frac{\partial}{\partial t} - \boldsymbol{\nabla}\psi \times \hat{\mathbf{z}} \cdot \boldsymbol{\nabla}\right)\omega = 0, \quad \nabla^2 \psi = \omega, \tag{1}$$

where ψ is the stream function, $\mathbf{v} = -\boldsymbol{\nabla}\psi \times \hat{\mathbf{z}}$ is the flow velocity, and $\omega = \boldsymbol{\nabla} \times \mathbf{v}$ is the vorticity, or local rotation rate of the fluid. Variants of Eqs. (1) are used widely to model geophysical [29–32] and astrophysical [33,34] fluids as well as strongly magnetized plasmas [23,35–37]. The (generalized) vorticity in such systems has a tendency to self-organize into stable, quasiaxisymmetric clumps which are commonly known as vortices. However, these structures are often embedded in external flow patterns due to boundaries and/or other vortices, which can cause them to deform. Shear and strain flows are the lowest-order local approximations to the external flow with nonzero velocity gradient, and are therefore expected to have the strongest influence. Thus, developing a precise understanding of the stability and dynamics of vortices in response to external flows is an important goal. This is particularly true in the context of fluid turbulence where nonlinear vortex interactions are strong and frequent, and persistent vortices are a source of intermittency that frustrates attempts at homogeneous modeling [38].

Non-neutral pure electron plasmas present a unique opportunity to study ideal 2D fluids experimentally due to weak dissipation, precise electrical control over boundary conditions, and ease of high-resolution diagnosis using a phosphor screen and a CCD camera [39–41]. The fluid-like behavior of such plasmas is due to a mathematical isomorphism between the Drift-Poisson equations describing the $\mathbf{E} \times \mathbf{B}$ drift dynamics of the electrons perpendicular to the strong magnetic field and the 2D Euler equations (1) describing ideal fluids [19,20]. This analogy has facilitated significant

progress in 2D vortex dynamics, including studies of vortex merging [42–44], the formation of vortex crystals [45,46], and a variety of other interesting results. By manipulating the boundary conditions of the plasma containment device using the rotating wall technique [47–49], electron vortices can be prepared with quasiflat, patchlike vorticity profiles. Recently, the boundary control capability has been used to subject these vortices to external strain flows, providing an experimental test of the vortex patch model under constant strain [50,51]. Here we extend these studies to the case of time-dependent strain, for which adiabatic evolution is perhaps the simplest example.

Steady, nonaxisymmetric electron plasmas have been produced and studied previously [52–54], and adiabatic behavior of diocotron modes with azimuthal wave number $m = 1$ has been investigated [8,53] (in contrast with the $m = 2$ elliptical deformations studied here). However, these experiments were not consistent with a rigorous 2D fluid description due to the low aspect ratio of the confinement device. Adiabaticity is often presented using the example of a harmonic oscillator where the frequency varies smoothly in time, resulting in exponential breaking. References [1,7,8] also consider nonanalytic (e.g., piecewise) ramps which give rise to power-law breaking curves. However, the more general case of adiabatic behavior involving an oscillator with both a driving term and frequency variation has not been discussed widely in the literature.

This paper is organized in the following way: In Sec. II the adiabatic breaking curves are computed analytically using the Kida elliptical vortex patch model along with a WKB approximation. In Sec. III details of the experimental procedure are given, including further discussion of the analogy between 2D fluids and electron plasmas. In Sec. IV the experimental data are presented and compared to the theoretical model. In Sec. V the results are discussed and compared with other related experimental, numerical, and theoretical work. Finally, in Sec. VI a summary is given along with an outlook toward future work.

II. THEORETICAL ANALYSIS

A. Details of the elliptical vortex patch model

The calculation that follows concerns vortex patches [14] subject to external strain flows in ideal 2D fluids described by Eqs. (1). The vorticity is treated as piecewise constant ω_0 inside an elliptical region, and zero elsewhere. The ellipse is described by an aspect ratio $\lambda \equiv a/b$ and an orientation ξ, where a and b are the semimajor and semiminor axes. Due to incompressibility, the area of the ellipse πab is a constant, but (λ, ξ) can evolve dynamically. The stream function and velocity field of the external strain flow are given by

$$\psi_{\text{ext}} = \tfrac{1}{2}\epsilon(x^2 - y^2), \quad \mathbf{v}_{\text{ext}} = \epsilon(y\hat{\mathbf{x}} + x\hat{\mathbf{y}}), \tag{2}$$

where ϵ is the strain rate and the strain axis (i.e., the direction of the positive eigenvector) is inclined at an angle $\pi/2$ relative to the x axis. The centroid of the ellipse is located at the origin, so $m = 1$ translational motion of the vortex does not occur.

For constant strain rates $d\epsilon/dt = 0$, Moore and Saffman [15] found stable and unstable equilibria of this system when the strain-to-vorticity ratio ϵ/ω_0 is below a critical threshold, whereas Kida [16] found exact dynamical solutions including stable and unstable orbits in phase space. These solutions can be thought of as generalizations of Kelvin's $m = 2$ vortex surface waves [14]. They correspond to the lowest-order deformation in the truncated moment model of vortex interactions given by Ref. [21]. This work showed that the strained vortex patch system can be described by the Hamiltonian

$$H(\lambda, \xi) = 2\epsilon \sin(2\xi)\frac{1 - \lambda^2}{\lambda} + 2 \ln\left[\frac{(1 + \lambda^2)}{\lambda}\right], \tag{3}$$

where ξ is defined relative to the strain axis, and all time and frequency scales (including the parameter ϵ) are henceforth normalized to the constant ω_0. The effect of external shear which was included in earlier analyses [15–17,21] is neglected here since the shear flow component is
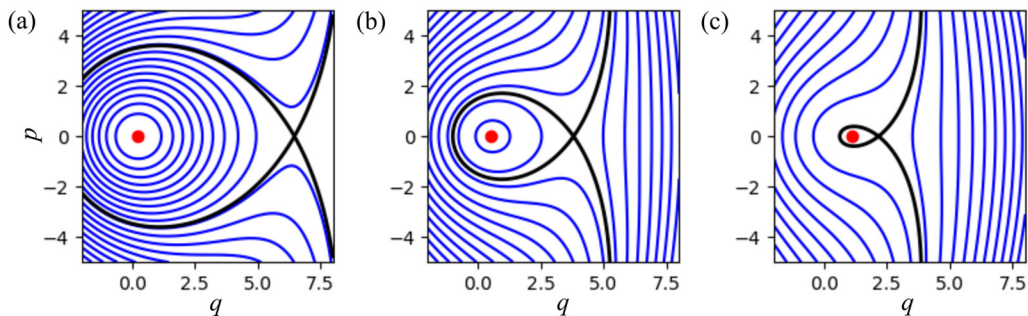
FIG. 1. Contours of H (blue lines) given by Eq. (5) are shown for $\epsilon =$ (a) 0.04, (b) 0.087, and (c) 0.14, along with the separatrix (thick black line) and center point (red dot). A saddle-node bifurcation occurs at $\epsilon_c \approx 0.15$. The initial condition $(p, q) = (0, 0)$ corresponding to a circular vortex loses stability at $\epsilon \approx 0.123$, between panels (b) and (c).

somewhat more difficult to produce experimentally than the strain. The orbits due to the external shear are similar to those due to the strain. The key qualitative difference is that the shear is a signed quantity either parallel or antiparallel to the vorticity, whereas a sign change of the strain rate amounts to a trivial $\pi/2$ rotation of the system.

Although (λ, ξ) are intuitive parameters of the ellipse geometry, they are not canonical variables of the system due to the symmetries $(\lambda, \xi) \to (1/\lambda, \ \xi + \pi/2)$ and $\xi \to \xi + \pi$. A suitable set of canonical variables and the corresponding Hamiltonian are given by [17]

$$(p, q) = \left[\frac{2(\lambda - 1)^2}{\lambda} \right]^{\frac{1}{2}} (\cos 2\xi, \ \sin 2\xi), \tag{4}$$

$$H(p, q) = 2 \ln \left(\frac{p^2 + q^2 + 8}{2} \right) - \epsilon q (p^2 + q^2 + 8)^{\frac{1}{2}}. \tag{5}$$

The phase portrait for Eq. (5) contains a stable center point and an unstable saddle point for small ϵ which undergo a saddle-node bifurcation at $\epsilon_c \approx 0.15$. The fixed points correspond to the steady elliptical equilibria described by Moore and Saffman [15]. The saddle defines a separatrix surrounding the center, inside which exist stable periodic orbits corresponding to the nutational or rotational motion described by Kida [16]. The frequency ν of the periodic orbits is a function of energy, approaching zero at the separatrix. Outside the separatrix are open orbits for which $\lambda(t) \to \infty$ as $t \to \infty$, meaning that the elliptical vortex is stretched indefinitely into a thin sheet, or "destroyed" due to the strain. For $\epsilon > \epsilon_c$ no stable orbits or equilibria exist. The phase portrait in terms of (p, q) is shown in Fig. 1 for a few values of the strain parameter ϵ including (b) the value $\epsilon_f = 0.087$ corresponding to the terminus of the ramps used in the experimental work.

When the strain rate in the Kida vortex patch model is taken to be a function of time, the dynamics given by Eq. (5) can be complicated and possibly chaotic [17]. However, when the strain varies slowly relative to the vortex rotation, the dynamics are constrained by the adiabatic theorem, which states that the action

$$I = \frac{1}{2\pi} \oint p \, dq \tag{6}$$

is an approximate constant of the motion provided that time-varying parameters in the Hamiltonian change slowly compared to the oscillation frequency ν, where the integral is evaluated over the cycle of a periodic orbit [2,3]. Validity of the adiabatic theorem is determined by the condition

$$\gamma \equiv \frac{1}{\nu} \frac{d\epsilon}{dt} \ll 1, \tag{7}$$

where γ is the dimensionless adiabaticity parameter that quantifies the separation of timescales between the oscillator and its changing environment. A system satisfying this condition behaves adiabatically when the change in the invariant $\Delta I = |I(t) - I(0)| \to 0$ as $\gamma \to 0$ over a sufficiently long time t. The invariant is said to be conserved to some order Z in the small parameter γ if $\Delta I \propto \gamma^Z$. Standard treatments of adiabaticity consider smooth, analytic ramp functions for the time-dependent parameter, for which I is conserved to all orders and so $\Delta I \propto \exp(-1/\gamma)$. Alternatively, ramps which are not infinitely differentiable result in finite Z and therefore power-law adiabatic breaking [1,7,8].

For this work, the initial conditions are taken as $\epsilon(t = 0) = 0$ and $\lambda(t = 0) = 1$ or $(p, q) = (0, 0)$, corresponding to an initially circular vortex in the absence of strain. This initial condition is chosen since axisymmetric vortices arise naturally in the experiments. Therefore, $I(t = 0) = 0$, and so adiabatic breaking results in small nonzero I associated with perturbative orbits about the center point as ϵ increases, where I corresponds to the amplitude of the orbit. Many studies of adiabatic systems focus on oscillations with finite initial amplitude where the normalized action $\Delta I/I$ is used as a breaking metric. This definition is not appropriate for the zero-amplitude, zero-strain initial condition considered here. Since adiabaticity is defined by the behavior of $\Delta I(\gamma)$ regardless of normalization [2,3], it is more useful to compare ΔI with the action at the separatrix, or that for which nonlinearity becomes important. This system can also exhibit adiabatic behavior when initiated at zero amplitude with finite strain, or at finite amplitude with zero strain. However, when initiated at zero amplitude (on the stable fixed point), frequency variation alone cannot cause adiabatic breaking; a driving term is required to displace the system from its equilibrium.

In the nonadiabatic limit $\gamma \to \infty$, the strain rate changes instantaneously from zero to some value ϵ. In this case the dynamics are simply given by the Kida solution [16] corresponding to Eq. (5) with constant ϵ and initial condition $(p, q) = (0, 0)$. The action I increases with ϵ as the fixed point is moved farther from the origin, until the orbit collides with the separatrix at $\epsilon \approx 0.123$ and loses stability. Further details of this situation and corresponding electron plasma experiments are presented in Refs. [50,51].

The strategy of the adiabatic breaking calculation is as follows. First, the frequency and fixed point location are expanded in ϵ, and small-amplitude excursions about the fixed point are assumed, yielding a harmonic system with a driving term and time-varying frequency. Second, solutions for the driven system are written in terms of the homogeneous solutions using the Green's function for a general second-order initial value problem. Here we consider two types of ramp function for the strain $\epsilon(t)$, a smooth hyperbolic tangent function given by

$$\epsilon(t) = \frac{1}{2}\epsilon_\text{f}\left[1 + \tanh\left(\frac{t - t_0}{\tau}\right)\right], \tag{8}$$

and a piecewise (nonanalytic) linear ramp function given by

$$\epsilon(t) = \begin{cases} \epsilon_\text{f} t/t_\text{f}, & (0 \leqslant t < t_\text{f}) \\ \epsilon_\text{f}, & (t \geqslant t_\text{f}), \end{cases} \tag{9}$$

where t_0, τ, t_f, and ϵ_f are constant parameters. In the case of the linear ramp, the homogeneous solutions are expressed using a WKB expansion to account for slow frequency variation, and the resulting equations are integrated in order to arrive at approximate analytical expressions for the adiabatic breaking.

B. Expansion about the stable equilibrium

Fixed points (p_0, q_0) of the Kida system are found by differentiating Eq. (5), resulting in $p_0 = 0$ and $q_0 > 0$ given by the solution to

$$q_0^6 + 16q_0^4 + 4(20 - 1/\epsilon^2)q_0^2 + 128 = 0. \tag{10}$$
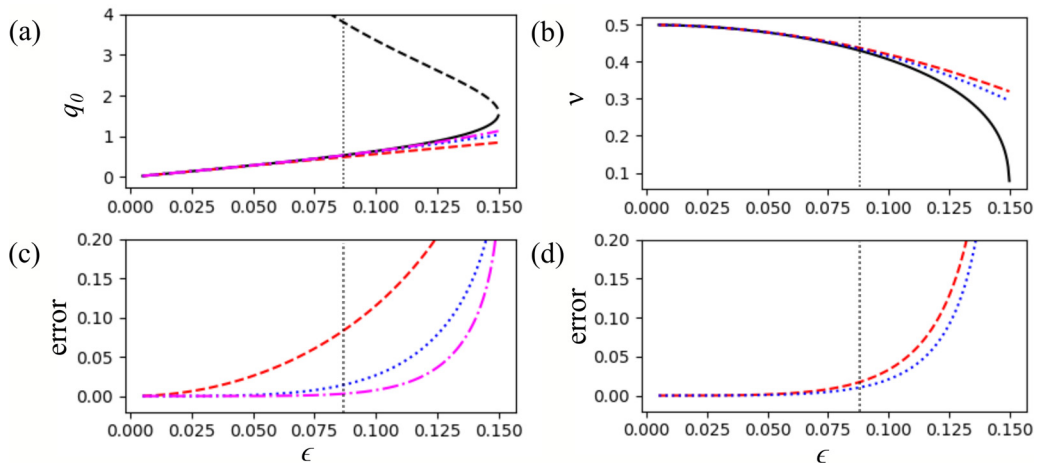
FIG. 2. Accuracy of approximations used in the calculation. (a) Center point locations q_0 given by Eq. (11) at first (dashed red), third (dotted blue), and fifth (dash-dot magenta) order in ϵ are compared to the solution of Eq. (10) for the center point (solid black) and the saddle point (dashed black). (b) The oscillation frequency ν given by Eq. (15) at second (dashed red) and fourth (dotted blue) order in ϵ are compared to the numerical solution (black). The relative errors of the approximations to (c) q_0 and (d) ν are given. The maximum strain $\epsilon_f = 0.087$ used in the experiments is indicated in each panel (dotted, vertical).

Expanding Eq. (10) in small ϵ yields

$$q_0 \approx 4\sqrt{2}[\epsilon + 10\epsilon^3 + 214\epsilon^5 + O(\epsilon^7)]. \tag{11}$$

The accuracy of the different orders of approximation to $q_0(\epsilon)$ is shown in Fig. 2(a) by comparing to the solution of Eq. (10). For small perturbations about the center point $(p, q) = (p_0 + \delta p, q_0 + \delta q)$ such that

$$\left| \frac{H(p, q) - H_0}{H_\times - H_0} \right| \ll 1, \tag{12}$$

where $H_\times$ and H_0 are the energy at the saddle and center point, respectively, Eq. (5) can be expanded at second order to yield

$$H_2 = H_0 + \frac{1}{2}A(\epsilon)[q - q_0(\epsilon)]^2 + \frac{1}{2}B(\epsilon)p^2, \tag{13}$$

where

$$A(\epsilon) = \frac{1}{2}\left.\frac{\partial^2 H}{\partial q^2}\right|_{(p_0,q_0)} \approx \frac{1}{2}[1 - 24\epsilon^2 - 240\epsilon^4 + O(\epsilon^6)],$$

$$B(\epsilon) = \frac{1}{2}\left.\frac{\partial^2 H}{\partial p^2}\right|_{(p_0,q_0)} \approx \frac{1}{2}[1 - 8\epsilon^2 - 96\epsilon^4 + O(\epsilon^6)]. \tag{14}$$

Equation (13) describes driven harmonic motion with frequency

$$\nu = (AB)^{\frac{1}{2}} \approx \nu_0[1 - 16\epsilon^2 - 100\epsilon^4 + O(\epsilon^6)], \tag{15}$$

where $\nu_0 = 1/2$ is the linear frequency for small amplitude $m = 2$ Kelvin waves when $\epsilon \to 0$ [14] [note that a factor of 2 arises due to the relationship between ξ and (p, q)]. For a harmonic oscillator, Eq. (6) reduces to

$$I = H/\nu. \tag{16}$$
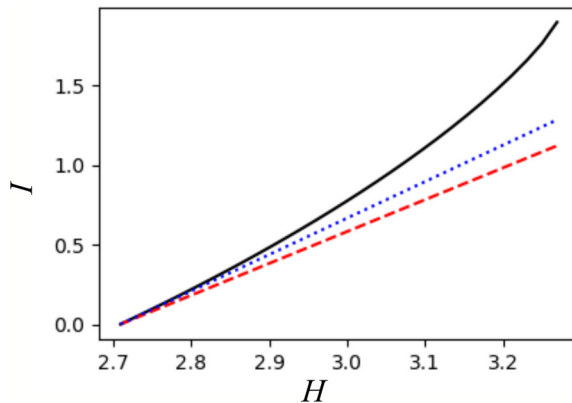
FIG. 3. The action I is plotted versus H for numerical solutions to Eq. (6) (solid black) and the harmonic oscillator formula, Eq. (16), where the frequency is approximated at zeroth (dashed red) and fourth (dotted blue) order in ϵ.

Since, at lowest nontrivial order q_0 is linear in ϵ whereas ν is quadratic, the driving term is expected to be the dominant source of adiabatic breaking.

The accuracy of the expansion in Eq. (15) is compared to the numerical solution in Fig. 2. The expansions of ν and q_0 lose convergence as the saddle-node bifurcation at $\epsilon_c \approx 0.15$ is approached, but for the maximum strain rate $\epsilon_f = 0.087$ used in the experiments presented here, they are appropriate. The accuracy of the harmonic oscillator approximation in Eq. (13) is shown in Fig. 3, where numerical solutions to Eq. (6) are plotted versus H from H_0 to $H_\times$, along with Eq. (16) where the frequency is approximated at zeroth and fourth order in ϵ. The harmonic approximation loses validity for larger amplitude orbits near the separatrix due to nonlinearity (as the orbits become nonelliptical). The largest value of action obtained in the experimental work due to adiabatic breaking is $I \approx 0.02$, whereas the action at the separatrix is $I \approx 1.9$ for $\epsilon_f = 0.087$, and so the harmonic approximation is well justified.

C. Solutions for the driven oscillator with constant frequency

Implementing Hamilton's equations, Eq. (13) is expressed as a linear second-order ordinary differential equation in self-adjoint form,

$$\frac{d}{dt}\left(\frac{\dot{q}}{B}\right) + Aq = Aq_0, \tag{17}$$

where $\dot{q} \equiv dq/dt$. The general solution is then given in terms of the homogeneous solutions q_1, q_2 by

$$q(t) = \int_{-\infty}^{t} dt' \, \nu^2(t') q_0(t') g(t, t'), \tag{18}$$

where

$$g(t, t') = \begin{cases} 0, & t < t' \\ \frac{q_1(t)q_2(t') - q_2(t)q_1(t')}{W(t')}, & t \geqslant t' \end{cases} \tag{19}$$

is the Green's function obtained by the method of variation of parameters, and

$$W(t) = \dot{q_1}(t)q_2(t) - \dot{q_2}(t)q_1(t) \propto B(t) \tag{20}$$

is the Wronskian. Through repeated integration by parts, Eq. (18) and its time derivative are expressed in a more convenient form:

$$q(t) - q_0(t) = \int_{-\infty}^{t} dt' \, \dot{q}_0(t') \frac{q_1(t)\dot{q}_2(t') - q_2(t)\dot{q}_1(t')}{W(t')}, \tag{21}$$

$$\dot{q}(t) = \int_{-\infty}^{t} dt' \, \dot{q}_0(t') \frac{\dot{q}_1(t)\dot{q}_2(t') - \dot{q}_2(t)\dot{q}_1(t')}{W(t')}. \tag{22}$$

Using these expressions, the action at time t can be evaluated as

$$I(t) = \frac{H}{\nu} = \frac{1}{2\nu}\left[A(q - q_0)^2 + \frac{\dot{q}^2}{B}\right], \tag{23}$$

where, in general, all quantities depend on time either directly or indirectly through $\epsilon(t)$.

At lowest order in ϵ, $q_0 = 4\sqrt{2}\,\epsilon$ and $\nu = \nu_0$, so the frequency is constant and the adiabatic breaking is due entirely to the driving term. In this case the homogeneous solutions are $q_{1,2} = \exp(\pm i\nu t)$, and the action is given by

$$I = \frac{A}{2\nu}\left|\int_{-\infty}^{t} dt' \, \exp(i\nu t')\dot{q}_0(t')\right|^2. \tag{24}$$

For the hyperbolic tangent ramp defined by Eq. (8), evaluation of Eq. (24) at $t \to \infty$ yields the action at lowest order

$$I(\tau) = \pi^2 \epsilon_{\mathrm{f}}^2 \tau^2 \mathrm{csch}^2\left(\frac{\pi \nu_0 \tau}{2}\right). \tag{25}$$

For the linear ramp defined by Eq. (9), this calculation gives the action at second order in the small parameter $\epsilon_{\mathrm{f}}/t_{\mathrm{f}}$ at time $t \geqslant t_{\mathrm{f}}$,

$$I_2(t_{\mathrm{f}}) = 256\left(\frac{\epsilon_{\mathrm{f}}}{t_{\mathrm{f}}}\right)^2 \sin^2\left(\frac{\nu_0 t_{\mathrm{f}}}{2}\right). \tag{26}$$

The breaking curve given by Eq. (25) for the smooth hyperbolic tangent ramp has the expected exponential behavior as $\tau \to \infty$, implying conservation of an adiabatic invariant to all orders in the small parameter γ. For the linear ramp, the breaking curve given by Eq. (26) is a power law $I \propto t_{\mathrm{f}}^{-2}$, with periodic zeros corresponding to integer multiples of the $m = 2$ Kelvin wave period.

D. WKB solutions accounting for frequency variation

At higher order in ϵ, variation in the oscillation frequency must be taken into account, and so the homogeneous solutions are expressed using a WKB approximation of the form

$$q_{1,2}(t) = \left(\frac{B}{A}\right)^{\frac{1}{4}} \exp\left[\pm i \int_0^t \nu(t')\,dt'\right], \tag{27}$$

where $\nu(t)$ is given by Eq. (15). Inserting Eq. (27) into Eqs. (21) and (22) results in

$$q(t) = q_0(t)\int_{-\infty}^{t} dt' \, \dot{q}_0(t')\left[\left(\frac{BA'}{AB'}\right)^{\frac{1}{4}}\cos(\Phi - \Phi') + \left(\frac{\dot{B}'}{4B'^2} - \frac{\dot{A}'}{4A'B'}\right)\left(\frac{BB'}{AA'}\right)^{\frac{1}{4}}\sin(\Phi - \Phi')\right], \tag{28}$$

$$\dot{q}(t) = \int_{-\infty}^{t} dt' \, \dot{q}_0(t')\left(\frac{BB'}{AA'}\right)^{\frac{1}{4}}\left\{\left[\nu\nu' + \frac{(A\dot{B} - B\dot{A})(A'\dot{B}' - B'\dot{A}')}{16ABA'B'}\right]\frac{\sin(\Phi - \Phi')}{B'}\right.$$
$$\left. + \left(\frac{BB'}{AA'}\right)^{\frac{1}{4}}\left(\frac{\dot{A}'}{A} - \frac{\dot{B}'}{B}\right)\frac{A'}{4\nu'}\cos(\Phi - \Phi')\right\}, \tag{29}$$

where $A' \equiv A(t')$, $\dot{A}' \equiv dA'/dt'$, etc., and $\Phi \equiv \int \nu\,dt$.

Finally, choosing the linear ramp function defined by Eq. (9), all quantities in Eqs. (28) and (29) are expressed as functions of time at the desired order in the small parameter ϵ_f/t_f, and it is assumed that $\epsilon_f \ll 1$ and $\epsilon_f^2 t_f \ll 1$ as well. The integrals are performed analytically using symbolic mathematics software, and the action is evaluated using Eq. (23). The final action at fourth order is

$$
\begin{aligned}
I_4(t_f) = I_2(t_f) + \frac{512}{3}\left(\frac{\epsilon_f}{t_f}\right)^4 \sin\left(\frac{v_0 t_f}{2}\right)\Bigg[3(21t_f^2 - 304)\sin\left(\frac{v_0 t_f}{2}\right) \\
- 4t_f(t_f^2 - 54)\cos\left(\frac{v_0 t_f}{2}\right) + 12t_f\cos\left(\frac{3v_0 t_f}{2}\right),
\end{aligned}
\tag{30}
$$

where $I_2(t_f)$ is given by Eq. (26). Due to increasing complexity, higher-order expressions are not shown here. This procedure is useful for (piecewise) polynomial ramps such as Eq. (9) since the integrals can be expanded in the small parameter ϵ_f/t_f; however, such an expansion is not possible for the hyperbolic tangent ramp, and so the integrals are difficult to carry out. In Sec. IV the above formulas are compared to experimental data and numerical solutions of the Kida system defined by Eq. (5), and the results are discussed.

E. Generalization to smooth vorticity profiles

Due to its simplicity, the low-dimensional vortex patch model is a useful tool that can yield convenient analytical results. However, it is also a highly idealized description featuring an unphysical infinite vorticity gradient at the edge of the vortex. Thus, it is important to consider how adiabatic behavior might be studied theoretically when the vorticity profile is taken to be smooth, especially when comparing to experimental data such as presented in Sec. IV. Although a thorough treatment of this subject is outside the scope of the present work, two possible approaches are identified here.

One approach consists of approximating a smooth profile using multiple nested elliptical patches [12,55]. An equilibrium configuration can be found where each patch assumes a different aspect ratio. An adiabatic invariant associated with small-amplitude oscillations can be identified for each patch, and so the vortex as a whole approximately preserves the sum of these invariants. This technique can fail due to destabilization of outer low-vorticity patches [11,12], or due to neglect of $m > 2$ deformations which arise from interactions between the patches.

Another approach is to model the smooth vortex as a collection of point vortices (PVs) whose dynamics are described by the Hamiltonian [14]

$$
H = \Gamma \sum_{i=1}^{N} \psi_{ext}(\mathbf{r_i}, t) - \frac{\Gamma^2}{4\pi}\sum_{i=1}^{N}\sum_{j=1}^{N}(1 - \delta_{ij})G(\mathbf{r_i}, \mathbf{r_j}),
\tag{31}
$$

where Γ is the PV circulation, ψ_{ext} is the stream function associated with the boundary conditions, δ_{ij} is the Kronecker delta function, $G(\mathbf{r_i}, \mathbf{r_j}) = \ln|\mathbf{r_i} - \mathbf{r_j}|$ is the Green's function for the Poisson equation in two dimensions (assuming the PVs are far away from boundaries), and N is the total number of PVs. The canonical variables for this system are proportional to the spatial coordinates of the PVs, $(p_i, q_i) = \Gamma^{\frac{1}{2}}(y_i, x_i)$. In the limit $N \to \infty$, Eq. (31) closely approximates the dynamics of the 2D Euler equations (1) [56]. Within a steady elliptical vortex consisting of many PVs, the macroscopic PV motion is described by periodic orbits about the vortex center along elliptical streamlines. Thus, as the external strain is varied slowly, each PV approximately preserves its own adiabatic invariant given by Eq. (6), which is proportional to the area enclosed by the streamline it follows. The vortex as a whole then preserves their sum

$$
I = \frac{\Gamma}{2\pi}\sum_{i=1}^{N}\oint y_i \, dx_i.
\tag{32}
$$

The assumption of adiabaticity fails when the PV orbits become sufficiently slow, which may occur for the outermost PVs nearest to the stream function separatrix, and so adiabatic breaking is expected to be strongest for the outer part of the distribution.

Using approximate models of smooth vortices such as multiple nested elliptical patches or point-vortex distributions in the large N limit, the notion of vortex adiabaticity can be extended to smooth vorticity profiles, at the cost of higher dimensionality relative to the simple elliptical patch model described by Eq. (5). These descriptions should reduce to the results of the single patch model described above when the spacing between the multiple patches vanishes, or when the PVs are arranged uniformly in an elliptical region.

III. EXPERIMENTAL PROCEDURE

A. The analogy between electron plasma and 2D fluid

The correspondence between magnetized electron plasma and ideal 2D fluid has been discussed extensively in the literature [20,23,39,43,45,50,57,58], and so only a brief review is given here. Typically, these experiments use a cylindrical electrode structure called a Penning-Malmberg trap where electron confinement is achieved using an applied magnetic field $\mathbf{B} = B\hat{\mathbf{z}}$ and an electrostatic potential well $\phi(z)$ [59,60]. Electrons in the trap bounce axially between the electrostatic barriers at frequency $f_b = \bar{v}/2L$ where $\bar{v} = \sqrt{T/m}$ is the thermal velocity, T and m are the electron temperature and mass, and L is the trap length. Perpendicular to the magnetic field, they perform small-scale, high-frequency gyro-orbits (also known as cyclotron orbits) at frequency $f_g = eB/m$ where e is the electron charge, as well as slower guiding-center drift motion with velocity (SI units) [5]

$$\mathbf{v} = \frac{\mathbf{E} \times \mathbf{B}}{B^2} = -\frac{\nabla\phi \times \hat{\mathbf{z}}}{B},\tag{33}$$

where $\mathbf{E}$ is the electric field. The cylindrical distribution of electrons creates a radial electric field which causes it to rotate due to the drift motion at the characteristic "vortex" frequency $f_v = en/2\epsilon_0 B$, where ε_0 is the permittivity of free space and n is the electron density. Dissipation is caused by like-particle collisions which occur at a rate per particle given roughly by $f_c = n\bar{v}e^4/T^2$ [61]. In typical conditions the frequency scales are ordered as

$$f_g \gg f_b \gg f_v \gg f_c,\tag{34}$$

and the spatial scales are ordered as

$$r_g \ll r_v < r_w \ll L,\tag{35}$$

where $r_g = \bar{v}/f_g$ is the gyro-radius, r_v is the characteristic scale of the drift motion (e.g., the vortex or plasma radius), and r_w is the inner wall radius of the cylindrical trap. These conditions are met primarily due to relatively low plasma density, high magnetic field, and high trap aspect ratio L/r_w. Therefore, on the frequency scale f_v, the rapid bounce motion and gyro-motion can be time-averaged and the dissipation neglected, resulting in a description of the electrons as thin, collisionless cylinders of charge of radius r_g drifting about the trap.

Under the orderings (34) and (35), the electron drift dynamics are described by the point vortex Hamiltonian given by Eq. (31), where the circulation Γ is replaced with the charge per length e/L and the stream function due to the boundary ψ_{ext} is replaced with the electric potential ϕ_{ext} [60]. Thus, the dynamics of the individual electrons are analogous to those of point vortices in an ideal 2D fluid. Similarly, the adiabatic invariants associated with individual point vortices are identified as the magnetic flux invariants of the charged particle motion, which are proportional to the area enclosed by the drift orbits when the magnetic field is constant [5,8]. When the density is sufficiently high, the electrons can be treated as a continuum represented by $n(x, y)$, just as a collection of point vortices can be approximated by a smooth vorticity function $\omega(x, y)$ [56]. In the continuum limit, the drift
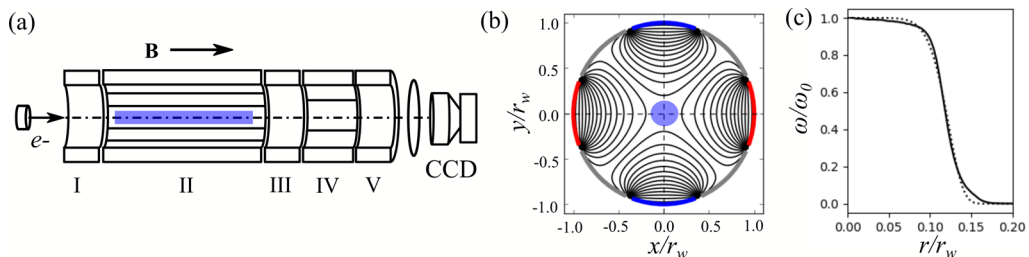
FIG. 4. The 8ST experimental apparatus. (a) A schematic diagram of the electrode structure, including solid electrodes I, III, and V, the eight-segment electrode II, and a four-segment electrode IV. Also shown are the electron gun (left), the phosphor screen and CCD camera diagnostic (right), and the plasma (blue). (b) A diagram of the segments of electrode II electrically biased in a quadrupole pattern with voltages $+V$ (red), $-V$ (blue), and 0 (gray), the resulting streamlines of the $\mathbf{E} \times \mathbf{B}$ strain flow (black), and the initially circular plasma (blue). (c) Measured initial radial vorticity profile (solid) and a fit function (dotted, see text for details).

dynamics are described by the drift-Poisson equations

$$\left(\partial_t - \frac{1}{B}\nabla\phi \times \hat{\mathbf{z}} \cdot \nabla\right)n = 0; \quad \nabla^2\phi = \frac{en}{\varepsilon_0}, \tag{36}$$

where all quantities are independent of the axial coordinate z. Equations (36) are isomorphic to Eqs. (1) under the transformations $\omega \to en/\varepsilon_0 B$ and $\psi \to \phi/B$ [19,20]. In this way, ideal 2D fluids obeying Euler equations can be studied in the laboratory by using pure electron plasmas as a proxy system, where the electron density is analogous to the fluid vorticity and the electric potential is analogous to the fluid stream function. Advantages of using electron plasmas to study 2D fluids include precise electrical control over the initial conditions and boundaries [41,49,53,62], the ability to rapidly vary experimental parameters (e.g., relative to water tank experiments [63] or numerical methods), and very weak dissipation.

B. The eight-segment trap apparatus

The experiments presented here use a specialized Penning-Malmberg device called the eight-segment trap (8ST) [41,50,51,64] in which an electrode with eight azimuthal segments extends over the entire plasma length, thus allowing for the imposition of boundary conditions $\phi_{\text{ext}}(r_w, \theta)$ while preserving the 2D fluid dynamics. The apparatus is shown schematically in Fig. 4(a), including a heated-cathode electron gun (left), solid confinement electrodes (I, III, V), the eight-segment electrode (II), a four-segment electrode (IV), and a diagnostic consisting of a phosphor screen and a CCD camera (right). The entire electrode structure is 0.44 m in length, electrode II is 0.26 m in length, the inner radius of the electrodes is $r_w = 13$ mm, the applied magnetic field is $B = 4.8$ T, and the system is held at ultrahigh vacuum conditions with pressure $\sim 10^{-9}$ torr. The plasmas described here have temperature $T \sim 0.1$ eV, length $L \approx 0.24$ m, particle number $N \approx 1.2 \times 10^8$, and density $n \approx 5.8 \times 10^{13}$ m^{-3}, and so $f_g = 134$ GHz, $f_b \approx 300$ kHz, and $f_v \sim 20$ kHz, $f_c \sim 3$ kHz, and the assumptions given in Eqs. (34) and (35) regarding the plasma/fluid correspondence are satisfied to at least an order of magnitude.

The segments of electrode II are electrically biased to voltages $(V, 0, -V, 0, V, 0, -V, 0)$ beginning along the positive x axis, as shown in Fig. 4(b). This produces an approximately quadrupolar potential near the origin which gives rise to an $\mathbf{E} \times \mathbf{B}$ strain flow of the same form as Eq. (2), where $\epsilon \approx 1.8V/\varepsilon_0 Br_w^2$ is the strain rate [41]. By varying the applied voltage V over time, the strain rate is ramped according to a smooth hyperbolic tangent given by Eq. (8) or a piecewise linear ramp function given by Eq. (9), where the final (maximum) strain is $\epsilon_{\text{f}} = 0.087$ for all data presented here. This value was chosen to be large enough to produce significant elliptical distortions with $\lambda \sim 1.5$, yet small enough to avoid nonlinear effects and separatrix crossing near the elliptical vortex patch
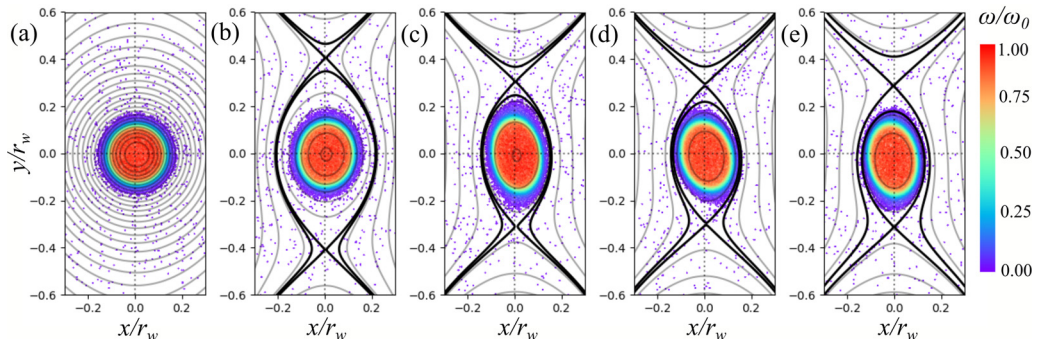
FIG. 5. Measurements of the vorticity (color map) are shown along with calculations of the stream function (gray lines) and its separatrix (thick black line) for a strain flow where the strain rate is ramped according to a hyperbolic tangent function given by Eq. (8) with $t_0 = 24.1$, $\tau = 8.76$, and $t = $ (a) 13.1, (b) 19.7, (c) 26.3, (d) 32.9, and (e) 39.4, corresponding to $\epsilon/\epsilon_f = $ (a) 0.08, (b) 0.27, (c) 0.62, (d) 0.88, and (e) 0.97. The vorticity data are truncated for $\omega/\omega_0 < 0.02$ to remove noise.

bifurcation at $\epsilon_c \approx 0.15$ [15]. For the hyperbolic tangent ramps, t_0/τ is chosen to be large enough that the discrete jump $\Delta\epsilon \sim 10^{-4}$ when the waveform is triggered at $t = 0$ is not important.

During an experimental run cycle, initial electron vortices are prepared with axisymmetric vorticity (density) profiles that are centered on the origin, as depicted in Fig. 4. First, electrons are injected into the trap using the heated cathode, and trapped between negatively biased electrodes I and V. Then any residual $m = 1$ diocotron oscillation [65] is damped using a feedback circuit applied to two of the four unused ($V = 0$) segments of electrode II, so as to position the plasma density centroid as close as possible to the origin. Next, the plasma density profile $n(r)$ is compressed and shaped using the rotating wall technique [66], where oscillating electric potentials are applied to electrode IV. Finally, the confinement region is shortened by negatively biasing electrode III such that the plasma is isolated under electrode II (the remaining plasma in the electrode IV region is discarded). For the data presented here, the vorticity profile is closely approximated by $\omega(r) = \omega_0 \exp[-(r/r_v)^\alpha]$, where the peak vorticity is $\omega_0 = 219$ krad/s, the vortex radius is $r_v = 1.63$ mm, and the smoothness parameter is $\alpha \approx 8$, as shown in Fig. 4(c).

Once the desired initial vortex is obtained, the external strain flow is applied and the vorticity $\omega(x, y)$ is allowed to evolve for some time, until it is diagnosed destructively by accelerating the plasma onto a phosphor screen biased to $+5$ kV. The resulting light is imaged with a CCD camera with pixel size $r_{pix} = 47$ μm and peak signal-to-noise ratio $\sim 10^2$. From this measurement and knowledge of the boundary conditions, the Poisson equation is solved numerically to determine the entire flow field $\psi(r \leqslant r_w, \theta)$. Ellipses are fit numerically using a least-squares routine to the half-maximum vorticity contour (using pixels with $0.4 < \omega/\omega_0 < 0.6$), providing measurements of the aspect ratio λ and orientation ξ of the elliptical deformations [41]. Run cycles are repeated at roughly 15 s intervals in order to build up time-series data. An example of vorticity and stream function measurements over time is shown in Fig. 5 for a hyperbolic tangent ramp function given by Eq. (8) with $t_0 = 24.1$, $\tau = 8.76$, and $t = 13.1 - 39.4$. As the strain grows over time, the vorticity assumes an approximately elliptical shape enclosed within the stream function separatrix, featuring small deviations from a steady elliptical equilibrium [15] with orientation $\xi = \pi/4$ relative to the strain axis.

C. Discussion of nonideal effects and systematic errors

The experimental methods discussed here are subject to two categories of errors. The first type is due to insufficient separation of temporal and/or spatial scales as defined by Eqs. (34) and (35), which causes some level of inconsistency with the 2D Euler equations (1). The second type includes

systematic errors and uncertainties that arise within the context of ideal 2D fluid dynamics. While many of these issues are discussed in Refs. [41,67], here we address those which are most relevant to the present work.

Dissipation in pure electron plasmas, although weak and often negligible for fluid experiments, differs in important ways from viscosity in traditional fluids described by the Navier-Stokes equations. On sufficiently long timescales $t > 1/f_c$, electron collisions result in viscous momentum transport [68]. However, since the viscosity is related to the electron density (vorticity), irrotational regions of the flow outside of the plasma are inviscid. Furthermore, due to a strong constraint on the total angular momentum in an azimuthally symmetric trap, the plasma cannot expand radially [69], and so viscosity serves to redistribute rather than broaden the vorticity profile. In practice, small asymmetries in the trap construction (e.g., gaps between the segments of electrode II) cause slow radial expansion of the plasma [70]. The vortex Reynolds number, defined as the ratio of the characteristic expansion time of the vortex to its rotation period $1/f_v$, is of the order $\mathrm{Re} \sim 10^6$ for the plasmas studied here [41]. In addition, dissipation is expected due to discrete particle effects for vorticity features on spatial scales near the interparticle spacing $(nL)^{-1/2} \sim 0.2 \,\mu\mathrm{m} \sim 10^{-4} \, r_v$. This can be an important consideration when studying thin vorticity filaments [64], but less so for the large-scale $m = 2$ deformations studied here.

The 3D electric field used for axial confinement at the ends of the trap (near electrodes I and III) gives rise to an approximately uniform background $\mathbf{E} \times \mathbf{B}$ rotation known as the "magnetron" drift [71] at a frequency $\sim$150 Hz in the 8ST [41]. Although it is due to 3D physics associated with the finite aspect ratio L/r_w, at lowest order this effect amounts to the application of a background shear flow in two dimensions, which is weaker than the peak vorticity by at least two orders of magnitude. This could cause a slight change to the equilibrium aspect ratio of the elliptical vortex relative to the prediction of Eq. (10), although it is expected to be a small effect.

Within the context of ideal 2D fluids, the duration of the experiment is limited by a translational instability of the entire vortex due to the applied strain flow [51,54]. Since the strain flow geometry is hyperbolic, the wave number $m = 1$ component of the vortex motion is unstable, causing an exponentially growing displacement from the axis. When the vortex is sufficiently displaced, it is subject to higher-order terms in the applied flow due to the discrete wall segments, as well as image fields induced by proximity to the wall. Following the $m = 2$ strain flow, $m = 6$ is the next largest term in the applied potential, and so higher-order effects are weaker by a factor of $(r/r_w)^4$ [41]. Additionally, the lowest-order image field correction regarding $m = 2$ plasma distortions is of order $(r/r_w)^4$ [71]. In practice, a small DC voltage is applied to one unused ($V = 0$) segment of electrode II in order to carefully center the initial vortex on the saddle point of the strain flow, thus delaying the instability as long as possible. For the data presented here, the vortex displacements are kept below $r/r_w \sim 0.2$ for the duration of the fluid experiments, which ranges from 150–300 μs ($t = 32.9$–65.7) depending on the ramp parameters.

Finally, precise measurements of the aspect ratio and orientation of the elliptical vortex are required for studies of adiabaticity. The uncertainty of the least-squares fitting routine is found to be on the order of $\Delta \lambda$, $\Delta \xi \sim 10^{-3}$ based on adjustment of the arbitrarily chosen half-maximum vorticity window from $0.45 < \omega/\omega_0 < 0.55$ to $0.35 < \omega/\omega_0 < 0.65$. Reproducibility of the experimental runs is the dominant source of uncertainty, with errors on the order of 10^{-2}. This estimate represents an aggregate of many small errors over the course of the initial vortex preparation [41].

In summary, the 8ST has been carefully designed to minimize nonfluid and nonideal effects, allowing for precise study of vortex dynamics in the presence of external flows.

IV. EXPERIMENTAL DATA

Using the techniques described above in Sec. III, initially axisymmetric electron vortices with quasiflat vorticity profiles are subjected to external strain flows where the strain rate increases over time according to either a hyperbolic tangent or linear ramp function. The vortices deform elliptically in response to the strain flow, and the aspect ratio and orientation (λ, ξ) of the elliptical

FIG. 6. Measurements of (a), (b) the aspect ratio λ, (c), (d) the orientation ξ, (e), (f) the action I, and (g), (h) the corresponding hyperbolic tangent (left) and linear (right) ramp functions $\epsilon(t)$ given by Eqs. (8) and (9). For the hyperbolic tangent ramps $\tau = 4.38$ (blue circles), 8.76 (red triangles), and $t_0 = 19.7$, 24.1, respectively, and for the linear ramps $t_f = 9.86$ (blue circles) and 19.71 (red triangles). Also shown are (a)–(f) numerical solutions of the elliptical patch system given by Eq. (3) (solid lines) and (a)–(d) the equilibrium aspect ratio λ_0 and orientation ξ_0 (dashed) at (g), (h) the maximum strain $\epsilon_f = 0.087$ (dashed).

shapes are measured using a CCD camera diagnostic. The evolution of the experimental ellipse parameters is then compared to numerical solutions of the Kida elliptical vortex patch system defined by Eq. (3). Finally, the change in the adiabatic invariant I is computed from the experimental data and from the numerical solutions, and these are compared to the analytical results given in Sec. II.

Figure 6 shows experimental measurements and numerical simulations of λ, ξ, and I over time, as well as the ramp functions $\epsilon(t)$. The left and right columns show results for hyperbolic tangent ramp functions defined by Eq. (8) and linear ramp functions defined by Eq. (9), including two ramps which are relatively slow and fast for each case. At late times $(t - t_0)/\tau \gg 1$ in the former case and $t > t_f$ in the latter, the ellipse parameters oscillate about their equilibrium values. The slower hyperbolic tangent ramp results in smaller amplitude oscillations and therefore lower final action compared to the faster ramp, as expected for an adiabatic system. The same trend is observed for the linear ramps, although the difference between the fast and slow ramps is relatively small once both have concluded. The slower linear ramp features a local minimum in the action at time $t \approx 2\pi/\nu_0$ corresponding to the first complete oscillation of the ellipse parameters, which is absent for the faster ramp where $t_f < 2\pi/\nu_0$.

The orbit trajectories in (p, q) space corresponding to the data in Fig. 6 are plotted in Fig. 7 for $t > t_f$ (linear ramp) or $t > t_{98}$ (hyperbolic tangent ramp), where $t_{98} \equiv t(\epsilon = 0.98\epsilon_f)$ is chosen arbitrarily as the effective terminus of the smooth ramp. The orbits spiral inward over time toward the stable fixed point, corresponding to a decrease in the action relative to the constant-energy orbits defined by Eq. (5). This behavior can also be observed in Fig. 6 where the action decreases over time relative to the numerical solution. This is thought to be due to a spatial Landau damping or critical-layer inviscid damping mechanism associated with the smooth edges, or finite vorticity gradient, of the experimental vortices [23–26] which is not realized in the elliptical patch model.
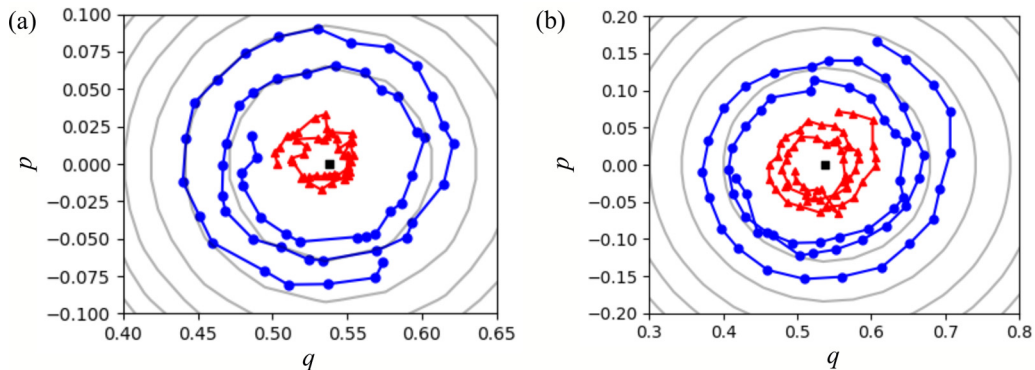
FIG. 7. Orbits in (p, q) space following the end of the ramp, for (a) hyperbolic tangent ramps with $t > t_{98}$ and (b) linear ramps with $t > t_f$. Parameters of the slow (red triangles) and fast (blue circles) ramps are identical to those in Fig. 6. Also shown are contours of H (gray) given by Eq. (5) and the location of the stable fixed point (black square) given by Eq. (10), for $\epsilon_f = 0.087$.

Here energy is transferred from the elliptical oscillation of the vortex core to the low-vorticity outer region at the "critical layer" where the fluid velocity is resonant with the oscillation. This behavior has been studied for elliptical electron plasma vortices in the absence of external flows [24]. It has also been observed in the 8ST for large-amplitude elliptical oscillations in the presence of strain [51]. Such damping appears to be a ubiquitous feature of nonaxisymmetric vortices with realistic smooth edges (e.g., when distorted due to external flows). Detailed investigation of this phenomenon is left for future work.

As an experimental measure of the adiabatic breaking, $I(t)$ is calculated using Eqs. (13)–(16) and averaged over the time window between t_{98} or t_f and the end of the data set. The measurements of $I(t)$ across this time window are shown in Fig. 8 for (a) the hyperbolic tangent and (b) the linear ramp function. All cases show an overall decrease in I over time, consistent with the critical-layer damping mechanism discussed above. For smaller action resulting from slower ramps, the data show higher uncertainty between experimental runs as discussed in Sec. III. Additionally, for the slower ramps, oscillations in $I(t)$ are observed at roughly the orbital frequency $2\pi/\nu_0$, which may be an indication of a mismatch between the orbit center and the fixed point location calculated by Eq. (10). Although the exact source of this error is not known, it could be due to uncertainty in the measurement of applied strain rate or vorticity [41], background shear due to the magnetron drift associated with 3D electric fields at the end of the trap (see Sec. III), or possibly smooth-profile effects involving the influence of the low-vorticity outer region on the vortex core [55].

The time-averaged measurements of the action I following conclusion of the ramps are plotted versus the ramp rate in Fig. 8 for (c) hyperbolic tangent and (d) linear ramp functions, along with the adiabatic breaking curves calculated in Sec. II and those obtained with numerical solutions to the elliptical patch model defined by Eq. (5). For the hyperbolic tangent ramp, the data show standard exponential breaking for $\tau \lesssim 7$ as expected. However, they are shifted toward lower action relative to the prediction of Eq. (25) and that of the numerical model, probably due to critical-layer damping. For slower ramps and smaller action, the data approach a constant value of $I \sim 10^{-4}$, which likely indicates the noise floor due to measurement uncertainty associated with the finite pixel resolution of the CCD camera and/or errors in the least-squares ellipse fitting routine, as discussed in Sec. III. Note that this value is similar to that observed for quasiaxisymmetric vortices early in the hyperbolic tangent ramps shown in Fig. 6(e), where it is expected that $I = 0$. The analytical prediction of Eq. (25) is slightly lower than that of the numerical model due to neglecting of frequency variation.

For the linear ramp function, the breaking curve is periodic within a power-law envelope with an exponent of about -2 on both the upper and lower bound. The data are in close agreement with the
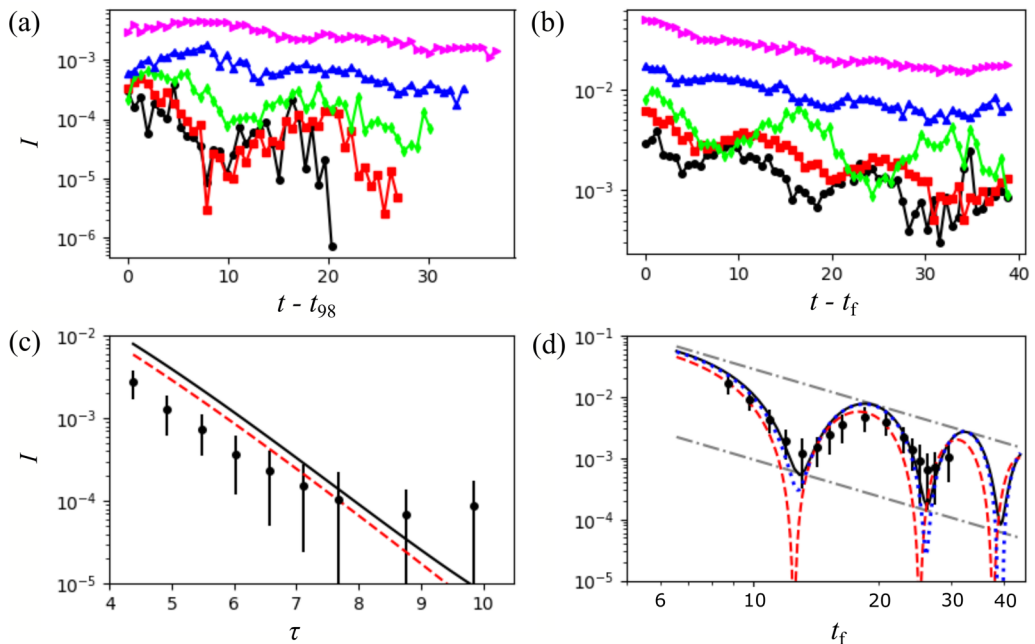
FIG. 8. (a), (b) Measurements of $I(t)$ following the end of the ramps defined by t_{98} for hyperbolic tangent functions (left) with $\tau = 4.38$ (magenta triangles), 5.48 (blue triangles), 6.57 (green diamonds), 7.67 (red squares), and 9.86 (black circles), and t_f for linear functions (right) with $t_f = 6.57$ (magenta triangles), 8.76 (blue triangles), 10.95 (green diamonds), 16.43 (red squares), and 21.9 (black circles). (c), (d) Adiabatic breaking curves, where measurements of I are averaged over the time windows in (a), (b) and plotted versus the ramp rates τ and t_f. Also shown in (c), (d) are numerical solutions of the elliptical vortex patch system given by Eq. (5) (solid black), the analytical predictions of Eqs. (25) and (26) for constant frequency (dashed red), the sixth-order WKB solution (dotted blue), and t_f^{-2} curves (dash-dot gray).

numerical model except that the minima and maxima are somewhat less extreme, possibly due to smooth profile effects such as critical-layer damping. The constant-frequency solution of Eq. (26) accounts for the majority of the breaking, although the period is shorter since $d\nu/d\epsilon < 0$. The WKB solution (shown here up to sixth order in ϵ) more accurately predicts the periodicity and breaking amplitude, except in narrow regions near the minima where the error increases with t_f due to neglect of higher-order terms.

V. DISCUSSION

Here we have utilized the Kida equations describing an elliptical vortex patch in a strain flow [16,17] in order to model the time-dependent behavior of a vortex as the strain is slowly turned on. Experiments using electron plasmas have verified much of the analysis, including the predominant effect of the driving term on the breaking of an adiabatic invariant related to periodic vortex oscillations. In this section, we discuss these conclusions with respect to previous work.

Adiabatic behavior in the context of the Kida elliptical vortex patch model appears to have been first studied using numerical experiments in Ref. [13]. Here image vorticity was induced in a nearby boundary, causing the vortex patch to experience a shear flow at lowest order. The shearing rate was varied temporarily as the vortex moved past a boundary feature, resulting in standard exponential breaking of an adiabatic invariant, provided the vortex was sufficiently far from the boundary. The experimental and theoretical work discussed above builds upon these ideas, providing a general framework for understanding and predicting the adiabatic evolution of 2D vortices in external

flows. By manipulating the boundary conditions directly, greater control over the properties of the external flow is possible. The effect of the shear flow considered previously [13] and the strain flow considered here on the vortex dynamics is expected to be qualitatively similar in the small-amplitude limit [16]. Although yet to be demonstrated experimentally, applied shear flows can probably be studied using the 8ST device by rotating the quadrupolar voltage pattern about the trap.

The behavior of a harmonic oscillator in response to frequency ramps of arbitrary form was studied in Ref. [1] using a WKB analysis. It was found that when the frequency variation has M continuous time derivatives, the adiabatic invariant is broken to $M + 1$ orders. In the work presented here for linear strain ramps, since $\nu(\epsilon) \propto \epsilon^2$ near $\epsilon = 0$, then $M = 1$ and the breaking due to frequency variation is expected to scale as t_f^{-2}, in agreement with the experimental and numerical results. However, the breaking shown in Fig. 8 is dominated by the driving term in the equations of motion, which was not considered in Ref. [1], and also scales as t_f^{-2} to lowest order.

Adiabaticity is often studied in the context of charged particle dynamics [5], typically either in astrophysical scenarios or laboratory devices. Nonanalytic ramps were studied numerically and theoretically in Ref. [7] with regard to electron gyro-motion subject to a changing magnetic field. Here the periodic modulation of the breaking curves observed in Fig. 8(d) was explained as originating from the relationship of the orbit period to the duration of the ramp. The periodic minima correspond to complete action integrals given by Eq. (6) where the oscillator phase is identical at the beginning and end of the ramp. When this condition is not met, then the incomplete portion of the integral contributes additional breaking. The local minimum in $I(t)$ observed in Fig. 6(f) is a further manifestation of this effect. Reference [7] also considered the influence of a driving term due to a shift in the electron guiding center as it travels through a flaring magnetic field, although they did not obtain analytic solutions in this case. Since the gyro-frequency is proportional to the magnetic field, adiabatic behavior is not possible when the field approaches zero. In contrast, it is possible here to study adiabatic ramps beginning at $\epsilon = 0$ since the orbital frequency of the vortex given by Eq. (15) is finite.

Similar adiabatic breaking curves were found in electron plasma experiments [8,53] regarding the $m = 1$ diocotron mode (analogous to vortex Kelvin waves), in which the plasma executes circular orbits about the trap due to image charge induced in the wall [65]. In this case the motion is translational and the plasma is treated as a point charge (elliptical deformations similar to those studied here were measured, but it was concluded that they were unimportant [8]). A wall segment was biased in order to deform the circular orbit adiabatically, where a linear ramp function resulted in power-law breaking with an exponent -1. The consistency of this behavior with the theoretical arguments of Ref. [1] appears to be a consequence of a linear relationship between the oscillator frequency and the segment voltage at finite amplitude, in contrast with the quadratic relationship given here by Eq. (15). Furthermore, the biased segment causes a shift of the orbit center [72], and therefore a driving term which was not considered in Ref. [8]. Finally, these experiments took place in a short trap with aspect ratio $L/r_w \sim 3$, and so they were inconsistent with the assumptions of the plasma/fluid analogy given by Eq. (35). A similar experiment obtained steady elliptical plasmas, where 3D effects were accounted for with an empirical parameter [54]. Here the stable fixed point described by Moore and Saffman [15] was derived independently, but adiabaticity was not discussed.

Many studies of adiabaticity, including those mentioned above [1,7,8], involve oscillators which are initiated at finite amplitude, for which the breaking depends on the initial phase. Alternatively, the experiments presented here are initiated at zero amplitude (i.e., beginning on the stable fixed point), in which case breaking is only possible with the inclusion of a driving term. This means that the initial phase is arbitrary, and so this extra degree of complication is absent in the present work.

Interestingly, the steady elliptical vortex patch equilibria found by Moore and Saffman [15] are identical to those of a steady elliptical current distribution in 2D ideal (nonresistive) magnetohydrodynamics (MHD) subject to an applied quadrupolar magnetic potential [73]. This correspondence arises because the current density j in the MHD system follows a Poisson equation $\nabla^2 \Psi = -\mu_0 j$ where μ_0 is the permeability of free space and Ψ is the magnetic scalar potential in two dimensions,

analogous to Eqs. (1) when the time derivative is set to zero. However, this correspondence is independent of the analogy between pure electron plasmas and ideal fluids, and it does not extend to dynamical behavior.

Similar adiabatic behavior can be expected in a variety of quasi-2D fluid and plasma systems related to Eqs. (1), ranging from geophysical and astrophysical fluids [29,33] to accelerator beams [37,65]. In particular, the Kida elliptical vortex patch model discussed here [16] has been implemented in the analysis of Earth's antarctic polar vortex [32] and geophysical storms elsewhere in the solar system [30,31], as well as in protoplanetary disks [34]. Interestingly, breaking curves resembling that in Fig. 8(d) have been obtained in quantum information experiments where trapped ions are adiabatically shuttled between different spatial regions [10]. These examples demonstrate the broad applicability of the adiabatic behavior studied here across a range of seemingly disparate disciplines.

VI. SUMMARY AND CONCLUSIONS

The experiments and theory presented here demonstrate adiabatic behavior associated with periodic, elliptical distortions of vortices in ideal 2D fluids or magnetized electron plasmas subject to slowly growing external strain flows. The adiabatic invariant is interpreted as the amplitude of a perturbative harmonic oscillation about a stable elliptical equilibrium which changes over time with the strain [15]. The experimental results largely agree with a simple vortex patch model [14,16,17,21], except that the realistic smooth vorticity profile causes inviscid critical-layer or Landau damping of the orbits [23–26]. The adiabatic breaking is due primarily to a driving term in the equations of motion which increases linearly with the strain, whereas the oscillation frequency varies quadratically with the strain and therefore plays a secondary role. Smooth, analytic ramp functions and piecewise, nonanalytic functions have been studied, where the former result in standard exponential breaking of the invariant and the latter give periodically modulated power-law breaking curves. These results are expected to be relevant to a wide variety of physical systems ranging from geophysical fluids [29–32] and astrophysical disks [33,34] to accelerator beams [37,65] and quantum information experiments [10].

Vortex dynamics subject to time-dependent external flows is a complicated subject with many aspects remaining to be understood. The scope can be narrowed by focusing on particular properties of the vortices, external flows, and time dependence. A distinct advantage can be gained by working with the elliptical vortex patch model, which reduces the problem to a one-dimensional Hamiltonian system [17]. However, it is important to understand how the vortex dynamics differ from the patch model when physically realistic, smooth vorticity profiles are considered. Gaussian vorticity profiles have been studied widely [11,12] since they arise naturally in fluids described by the Navier-Stokes equations (e.g., the Lamb-Oseen vortex [14]). The experiments presented here utilize quasiflat vorticity profiles with smooth edges which approximate the idealized vortex patch, thus offering a perturbative approach to understanding how finite vorticity gradients modify the patch behavior.

Studying slowly varying external flows offers another advantage, since adiabatic theory can be invoked. Thus, to lowest order, the dynamics are insensitive to the exact time dependence as long as it is sufficiently slow. However, the results shown here (as well as studies of other similar adiabatic systems [1,7,8,10]) indicate that higher-order adiabatic breaking depends in interesting ways on the time dependence considered. Such analyses are therefore an important step toward understanding the quasiadiabatic regime where the gap between the oscillator frequency and that of its changing environment narrows.

This work represents the latest step in a research program focusing on vortex dynamics in external flows using pure electron plasmas in the laboratory. Previous work has studied vortex dynamics and shear layers subject to constant strain flows [50,51,64], whereas the present work considers time-dependent external flows, for which adiabatic behavior is perhaps the simplest case. Interesting future directions of research include further studies of smooth-profile effects such as critical-layer

damping, studies of both external shear and strain flows, and more complicated functional forms of the time-dependent strain.

[1] R. M. Kulsrud, Adiabatic invariant of the harmonic oscillator, Phys. Rev. **106**, 205 (1957).

[2] H. Goldstein, C. Poole, and J. Safko, in *Classical Mechanics*, 3rd ed. (Addison-Wesley, San Francisco, 2002).

[3] C. G. Wells and S. T. C. Siklos, The adiabatic invariance of the action variable in classical dynamics, Eur. J. Phys. **28**, 105 (2006).

[4] T. G. Northrop, Adiabatic charged particle motion, Rev. Geophys. **1**, 283 (1963).

[5] F. F. Chen, *Introduction to Plasma Physics and Controlled Fusion*, 2nd ed. (Plenum Press, New York, 1984).

[6] T. M. O'Neil and P. G. Hjorth, Collisional dynamics of a strongly magnetized pure electon plasma, Phys. Fluids **28**, 3241 (1985).

[7] J. E. Borovsky and P. J. Hansen, Breaking of the first adiabatic invariants of charged particles in time-dependent magnetic fields: Computer simulations and theory, Phys. Rev. A **43**, 5605 (1991).

[8] J. Notte, J. Fajans, R. Chu, and J. S. Wurtele, Experimental Breaking of an Adiabatic Invariant, Phys. Rev. Lett. **70**, 3900 (1993).

[9] J. R. Cary and A. J. Brizard, Hamiltonian theory of guiding-center motion, Rev. Mod. Phys. **81**, 693 (2009).

[10] S. Schulz, U. Poschinger, K. Singer, and F. Schmidt-Kaler, Optimization of segmented linear paul traps and transport of stored particles, Fortschr. Phys. **54**, 648 (2006).

[11] A. Mariotti, B. Legras, and D. G. Dritschel, Vortex stripping and the erosion of coherent structures in two-dimensional flows, Phys. Fluids **6**, 3954 (1994).

[12] B. Legras, D. G. Dritschel, and P. Caillol, The erosion of a two-dimensional vortex in a background straining flow, J. Fluid Mech. **441**, 369 (2001).

[13] A. Crosby, E. R. Johnson, and P. J. Morrison, Deformation of vortex patches by boundaries, Phys. Fluids **25**, 023602 (2013).

[14] P. G. Saffman, *Vortex Dynamics* (Cambridge University Press, Cambridge, 1992).

[15] D. W. Moore and P. G. Saffman, Structure of a line vortex in an imposed strain, in *Aircraft Wake Turbulence and Its Detection*, edited by M. R. J. H. Olsen and A. Goldburg (Plenum Press, New York, 1971), pp. 339–354.

[16] S. Kida, Motion of an elliptic vortex in a uniform shear flow, J. Phys. Soc. Jpn. **50**, 3517 (1981).

[17] K. Ide and S. Wiggins, The dynamics of elliptically shaped regions of uniform vorticity in time-periodic, linear external velocity fields, Fluid Dyn. Res. **15**, 205 (1995).

[18] E. A. Ryzhov, Nonlinear dynamics of an elliptic vortex embedded in an oscillatory shear flow, Chaos **27**, 113101 (2017).

[19] R. H. Levy, Diocotron instability in a cylindrical geometry, Phys. Fluids **8**, 1288 (1965).

[20] C. F. Driscoll and K. S. Fine, Experiments on vortex dynamics in pure electron plasmas, Phys. Fluids B **2**, 1359 (1990).

[21] M. V. Melander, N. J. Zabusky, and A. S. Styczek, A moment model for vortex interactions of the two-dimensional Euler equations. Part 1. Computational validation of a Hamiltonian elliptical representation, J. Fluid Mech. **167**, 95 (1986).

[22] K. R. Symon, The adiabatic invariant of the linear or nonlinear oscillator, J. Math. Phys. **11**, 1320 (1970).

[23] R. J. Briggs, J. D. Daugherty, and R. H. Levy, Role of landau damping in crossed-field electron beams and inviscid shear flow, Phys. Fluids **13**, 421 (1970).

[24] D. A. Schecter, D. H. E. Dubin, A. C. Cass, C. F. Driscoll, I. M. Lansky, and T. M. O'Neil, Inviscid damping of asymmetries on a two-dimensional vortex, Phys. Fluids **12**, 2397 (2000).

[25] S. L. Dizes, Non-axisymmetric vortices in two-dimensional flows, J. Fluid Mech. **406**, 175 (2000).

[26] N. J. Balmforth, S. G. L. Smith, and W. R. Young, Disturbing vortices, J. Fluid Mech. **426**, 95 (2001).

[27] P. J. Morrison, Hamiltonian description of the ideal fluid, Rev. Mod. Phys. **70**, 467 (1998).

[28] P. Tabeling, Two-dimensional turbulence: A physicist approach, Phys. Rep. **362**, 1 (2002).

[29] D. G. Dritschel and B. Legras, Modeling oceanic and atmospheric vortices, Phys. Today **46**(3), 44 (1993).

[30] L. M. Polvani, J. Wisdom, E. DeJong, and A. P. Ingersoll, Simple dynamical models of Neptune's great dark spot, Science **249**, 1393 (1990).

[31] A. A. Simon, M. H. Wong, and A. I. Hsu, Formation of a new great dark spot on Neptune in 2018, Geophys. Res. Lett. **46**, 3108 (2019).

[32] M. Mester and J. G. Esler, Dynamical elliptical diagnostics of the antarctic polar vortex, J. Atmos. Sci. **77**, 1167 (2020).

[33] R. V. E. Lovelace, H. Li, S. A. Colgate, and A. F. Nelson, Rossby wave instability of Keplerian accretion disks, Astrophys. J. **513**, 805 (1999).

[34] P. J. Armitage, Physical processes in protoplanetary disks., in *From Protoplanetary Disks to Planet Formation*, edited by P. J. Armitage and Wilhelm Kley (Springer, Berlin, 2019), pp. 1–150.

[35] A. Hasegawa and K. Mima, Pseudo-three-dimensional turbulence in magnetized nonuniform plasma, Phys. Fluids **21**, 87 (1978).

[36] D. Montgomery and L. Turner, Two-dimensional electrostatic turbulence with variable density and pressure, Phys. Fluids **23**, 264 (1980).

[37] R. C. Davidson, H.-W. Chan, C. Chen, and S. Lund, Equilibrium and stability properties of intense non-neutral electron flow, Rev. Mod. Phys. **63**, 341 (1991).

[38] J. C. McWilliams, The emergence of isolated coherent vortices in turbulent flow, J. Fluid Mech. **146**, 21 (1984).

[39] D. Eggleston, Experimental study of two-dimensional electron vortex dynamics in an applied irrotational shear flow, Phys. Plasmas. **1**, 3850 (1994).

[40] D. Durkin and J. Fajans, Experiments on two-dimensional vortex patterns, Phys. Fluids **12**, 289 (2000).

[41] N. C. Hurst, J. R. Danielson, and C. M. Surko, An electron plasma experiment to study vortex dynamics subject to externally imposed flows, AIP Conf. Proc. **1928**, 020007 (2018).

[42] T. B. Mitchell and C. F. Driscoll, Electron vortex orbits and merger, Phys. Fluids **8**, 1828 (1996).

[43] M. Amoretti, D. Durkin, J. Fajans, R. Pozzoli, and M. Rome, Asymmetric vortex merger: Experiments and simulations, Phys. Plasmas **8**, 3865 (2001).

[44] Y. Soga, Y. Kiwamoto, A. Sanpei, and J. Aoki, Merger and binary structure formation of two discrete vortices in a background vorticity distribution of a pure electron plasma, Phys. Plasmas **10**, 3922 (2003).

[45] K. S. Fine, A. C. Cass, W. G. Flynn, and C. F. Driscoll, Relaxation of 2D Turbulence to Vortex Crystals, Phys. Rev. Lett. **75**, 3277 (1995).

[46] Y. Kiwamoto, N. Hashizume, Y. Soga, J. Aoki, and Y. Kawai, Formation and Relaxation of Two-Dimensional Vortex Crystals in a Magnetized Pure-Electron Plasma, Phys. Rev. Lett. **99**, 115002 (2007).

[47] X. P. Huang, F. Anderegg, E. M. Hollmann, C. F. Driscoll, and T. M. O'Neil, Steady-State Confinement of Non-Neutral Plasma by Rotating Electric Fields, Phys. Rev. Lett. **78**, 875 (1997).

[48] E. M. Hollmann, F. Anderegg, and C. F. Driscoll, Confinement and manipulation of non-neutral plasmas using rotating wall electric fields, Phys. Plasmas **7**, 2776 (2000).

[49] J. R. Danielson and C. M. Surko, Radial compression and torque-balanced steady states of single-component plasmas in Penning-Malmberg traps, Phys. Plasmas **13**, 055706 (2006).

[50] N. C. Hurst, J. R. Danielson, D. H. E. Dubin, and C. M. Surko, Evolution of a Vortex in a Strain Flow, Phys. Rev. Lett. **117**, 235001 (2016).

[51] N. C. Hurst, J. R. Danielson, D. H. E. Dubin, and C. M. Surko, Experimental study of the stability and dynamics of a 2D ideal vortex under external strain, J. Fluid Mech. **848**, 256 (2018).

[52] J. Notte, A. J. Peurrung, J. Fajans, R. Chu, and J. S. Wurtele, Asymmetric Stable Equilibria of Non-Neutral Plasmas, Phys. Rev. Lett. **69**, 3056 (1992).

[53] R. Chu, J. S. Wurtele, J. Notte, A. J. Peurrung, and J. Fajans, Pure electron plasmas in asymmetric traps, Phys. Fluids B **5**, 2378 (1993).

[54] J. Fajans, E. Y. Backhaus, and E. Gilson, Bifurcations in elliptical, asymmetric non-neutral plasmas, Phys. Plasmas **7**, 3929 (2000).

[55] L. M. Polvani and G. R. Flierl, Generalized Kirchoff vortices, Phys. Fluids **29**, 2376 (1986).

[56] J. Goodman, T. Y. Hou, and J. Lowengrub, Convergence of the point vortex method for the 2-D Euler equations, Comm. Pure Appl. Math. **43**, 415 (1990).

[57] D. H. E. Dubin, Collisional diffusion in a two-dimensional point vortex gas or a two-dimensional plasma, Phys. Plasmas **10**, 1338 (2003).

[58] S. Chen, G. Maero, and M. Rome, Spectral analysis of forced turbulence in a non-neutral plasma, J. Plasma Phys. **83**, 705830303 (2017).

[59] T. M. O'Neil, Trapped plasmas with a single sign of charge (from Coulomb crystals to 2D turbulence and vortex dynamics), Phys. Today **52**(2), 24 (1999).

[60] D. H. E. Dubin and T. M. O'Neil, Trapped nonneutral plasmas, liquids, and crystals (the thermal equilibrium states), Rev. Mod. Phys. **71**, 87 (1999).

[61] D. H. E. Dubin, Collisional transport in non-neutral plasmas, Phys. Plasmas **5**, 1688 (1998).

[62] D. Durkin and J. Fajans, Photocathode source for studying two-dimensional fluid phenomena with magnetized electron columns, Rev. Sci. Instrum. **70**, 4539 (1999).

[63] R. R. Trieling, M. Beckers, and G. J. F. V. Heijst, Dynamics of monopolar vortices in a strain flow, J. Fluid Mech. **345**, 165 (1997).

[64] N. C. Hurst, J. R. Danielson, D. H. E. Dubin, and C. M. Surko, Instability of an electron-plasma shear layer in an externally imposed strain flow, Phys. Plasmas **27**, 042101 (2020).

[65] R. C. Davidson, *Physics of Nonneutral Plasmas* (Addison-Wesley, Redwood City, CA, 1990).

[66] J. R. Danielson, T. R. Weber, and C. M. Surko, Plasma manipulation techniques for positron storage in a multicell trap, Phys. Plasmas **13**, 123502 (2006).

[67] A. J. Peurrung and J. Fajans, A limitation to the analogy between pure electron plasmas and two-dimensional inviscid fluids, Phys. Fluids B **5**, 4295 (1993).

[68] J. M. Kriesel and C. F. Driscoll, Measurements of Viscosity in Pure-Electron Plasmas, Phys. Rev. Lett. **87**, 135003 (2001).

[69] T. M. O'Neil, Cooling of a pure electron plasma by cyclotron radiation, Phys. Fluids **23**, 725 (1980).

[70] J. M. Kriesel and C. F. Driscoll, Two Regimes of Asymmetry-Induced Transport in Non-Neutral Plasmas, Phys. Rev. Lett. **85**, 2510 (2000).

[71] J. R. Danielson, D. H. E. Dubin, R. G. Greaves, and C. M. Surko, Plasma and trap-based techniques for science with positrons, Rev. Mod. Phys. **87**, 247 (2015).

[72] N. C. Hurst, J. R. Danielson, C. J. Baker, and C. M. Surko, Electron Plasma Orbits from Competing Diocotron Drifts, Phys. Rev. Lett. **113**, 025004 (2014).

[73] R. Gajewski, Magnetohydrodynamic equilibrium of an elliptical plasma cylinder, Phys. Fluids **15**, 70 (1972).